Blind Optical Aberration Correction by Exploring Geometric and Visual Priors

Tao Yue[1] Jinli Suo[1] Jue Wang[2] Xun Cao[3] Qionghai Dai[1]
[1]Department of Automation, Tsinghua University [2]Adobe Research
[3]School of Electronic Science and Engineering, Nanjing University

Abstract

Optical aberration widely exists in optical imaging systems, especially in consumer-level cameras. In contrast to previous solutions using hardware compensation or pre-calibration, we propose a computational approach for blind aberration removal from a single image, by exploring various geometric and visual priors. The global rotational symmetry allows us to transform the non-uniform degeneration into several uniform ones by the proposed radial splitting and warping technique. Locally, two types of symmetry constraints, i.e. central symmetry and reflection symmetry are defined as geometric priors in central and surrounding regions, respectively. Furthermore, by investigating the visual artifacts of aberration degenerated images captured by consumer-level cameras, the non-uniform distribution of sharpness across color channels and the image lattice is exploited as visual priors, resulting in a novel strategy to utilize the guidance from the sharpest channel and local image regions to improve the overall performance and robustness. Extensive evaluation on both real and synthetic data suggests that the proposed method outperforms the state-of-the-art techniques.

1. Introduction

Optical aberration is one of the most common sources of image degeneration that affects almost all lens-based imaging systems. High-end lens are carefully designed to reduce optical aberration. For example, the elements of the compound lens are made of different materials to compensate the imperfect refractive indices to reduce chromatic aberration. The surfaces of the singlet lenses are of different curvatures to compensate the imperfect focusing of the spherical lenses for educing the spherical, astigmatism and coma aberration. In general, better lens with less optical aberration are usually larger and cost much more to fabricate, thus may not applicable in consumer-level cameras. Researchers have also proposed various complex hardware solutions for compensating optical aberration [1, 9, 10, 15, 17, 18], but the requirement of using special devices limits their application range, especially for consumer applications.

Given the limitations of hardware solutions, computationally removing optical aberration has attracted strong interests and has been exensively studied in the past decade [3–5, 12, 13]. However, most of existing aberration correction methods [3, 5, 12] are *non-blind*, i.e. the Point Spread Functions (PSFs) of the aberration need to be calibrated beforehand. Kee *et al*. [5] propose a parameterized model to describe the nonuniform PSFs of a zoom lens at different focal lengths, so that only several calibration measurements are required to be taken. Schuler *et al*. [12] calibrate the nonuniform aberration PSFs using a grid of point light sources and apply the Efficient Filter Flow (EFF) method to perform efficient non-stationary deconvolution. Heide *et al*. [3] propose to reconstruct high quality images from aberration corrupted inputs captured by simple lenses, with the PSFs calibrated from the degenerated images of several random patterns. Instead of a fully pre-calibration of the PSFs, Shih *et al*. [14] only measure the PSF at a single depth, and then simulate the lens and trace the light rays to derive the whole PSF map computationally. The main advantage of these non-blind methods is that once the camera is well calibrated, the model can be applied to any input image given the optical aberrations are scene independent [20]. However the required calibration procedures usually demand expertise and special devices, thus largely limit their practical applications.

For *blind* aberration removal, Joshi *et al*. [4] propose a PSF estimation method by predicting sharp edges from blurry ones. Rahbar and Faez [11] use the Zernike model to describe the optical aberration and estimate the Zernike coefficients using Polyspectral analysis. However, they only deal with a single channel in this work and can not handle chromatic aberration. Recently, Schuler *et al*. [13] propose an orthonormal Efficient Filter Flow (EFF) basis based method which is built upon a series of assumptions. This

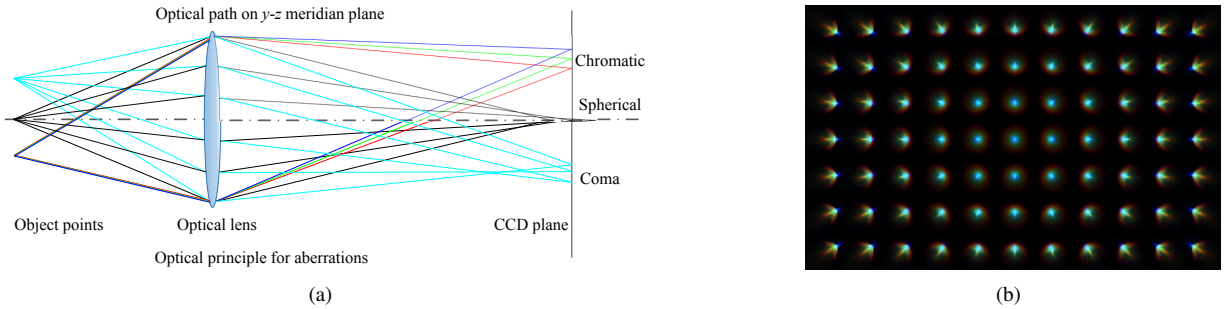

(a) (b)

Figure 1. The diagram of optical principle of (a) optical aberrations and (b) the resulting PSFs.

approach works well when the assumptions hold, but may fail in other cases, e.g., images with large spherical aberration, as we will show in our experiments. Tang and Kutulakos [16] prove that the blind recovery of both optical aberration and image depth from defocus blurred and aberration corrupted images is possible, and they use the Seidel model to approximate the aberration and simplify the problem. In general, blind aberration removal is more practical than non-blind compensation, but technically more challenging.

The goal of this work is to provide a better blind aberration correction method that achieves higher quality and better robustness/flexibility than previous approaches. Specifically, we first investigate the principle of optics and derive the geometric priors of the PSFs, including both the global rotational symmetry and the local reflectional/central symmetry. According to the global rotational symmetry, we propose a radial splitting and warping framework to transform the non-uniform aberrations in the concentric radial regions into spatially uniform blurs. This transform largely increases the efficiency and robustness of the algorithm, and allows us to incorporate mature techniques that are proven to be effective in uniform deblurring. In addition, we propose a more thorough local symmetry prior that includes both the reflection symmetry used in [13] and a central symmetry constraint. This enables us to handle both the off-axis PSFs (astigmatism and coma) and near-axis PSFs (spherical and chromatic).

Beside the geometric priors, we also introduces new visual priors. Inspired by the observation that in an optically aberrated image, sharpness varies spatially as well as across color channel, we propose to conduct both kernel estimation and deconvolution in a sharp-to-blur order. Specifically, we restore the sharpest channel and local region first, and then use the result to guide the processing of other regions and channels. The guidance is implemented via two visual priors of the degenerated images: cross-channel constraint on the latent sharp image and the smoothly-varying constraint on the blur kernels. This strategy and related visual priors significantly boost the performance of our method, especially for the seriously deteriorated images.

Compared with Schuler *et al*. [13]'s method, the proposed algorithm differs in three main aspects: (1) it can handle more types of aberrations across the image plane, especially the spherical aberration in the center region and coma in the surrounding regions. (2) Benefiting from the sharp-to-blur strategy, the proposed method achieves better performance and robustness, especially for the chromatic aberration. (3) The radial splitting and warping framework simplifies the problem and gives rise to a great potential in terms of computational efficiency.

2. Optics-inspired Geometric Priors of PSF

In this section, we analyze the principle of optics to derive the geometric priors of the aberration PSFs. Fig. 1(a) shows the light paths that cause the spherical, coma and chromatic aberrations. Generally, lens-based imaging systems are axisymmetric with respect to the optical axis, thus the light paths of a well manufactured consumer-level camera lens are also axis-symmetric, i.e., the off-axis points with the same distance to the optical axis have the same optical transform function (OTF). In addition, the OTF at a specific point should also be locally symmetric with respect to the line connecting it to the projection center, which we assume is the same as the image center. Neglecting the axis-asymmetric error due to imperfect lens manufacturing, all types of lens aberrations, e.g. spherical aberration, coma, and chromatic aberration, would cause PSFs that are globally rotational symmetric and locally central/reflective symmetric.

To describe these two geometric priors of PSFs, we propose a radial splitting and warping framework and a unified symmetry constraint, as described below.

Radial Splitting and Warping Framework The global rotational symmetry has been incorporated into a series of human designed basises in Schuler *et al*. [13]. In this work, we propose a radial splitting and warping framework that is more flexible than the EFF-basis-based method. Consid-

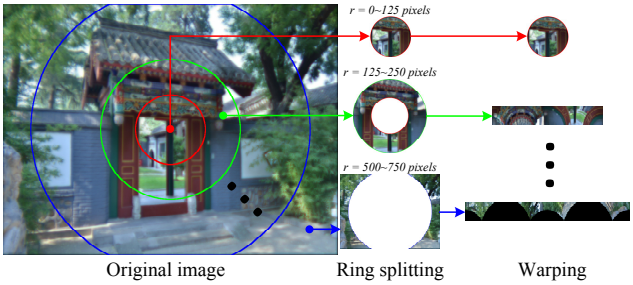

Figure 2. The diagram of the proposed concentric ringwise splitting and warping.

ering that the pixels in a narrow ring region have roughly the same PSF with different rotations, if we rotate the local patch of all pixels properly, the PSFs become uniform. Intuitively, by decomposing the image plane into a series of concentric ring regions, and further warping them into rectangular subimages, in which the y-axis is the radius dimension and the x-axis is the angular dimension, the non-uniform aberration becomes uniform in these rectangle subimages, as shown in Fig. 2. Each warped subimage thus can be handled by previous uniform PSF estimation and deconvolution algorithms. In this work we use Cho and Lee [2]'s approach for uniform PSF estimation and deconvolution given its good performance and high efficiency.

Fortunately, the PSFs caused by aberration are usually quite smooth, thus the sampling step during image warping does not affect the PSF estimation too much. To prevent from losing information caused by sampling and the following processing steps, we expand each subimage to make them partially overlap. For a ring region whose inner and outer radius are r_o and r_i, respectively, the width and height of the warped rectangular image is $W = 2\pi r_o \cdot c$ and $H = (r_o - r_i) \cdot c$, where $c = 1.1$ empirically. Here c is an over-sampling ratio to ensure all the image pixels are sampled at subpixel level. As a result, the sampling errors are generally at sub-pixel scale.

Symmetry Constraint For a point on the optical axis, the light paths through it are axis-symmetric, resulting in a central symmetric PSF (middle of Fig. 1(b)). For off-axis points, each light path across it has a reflection symmetric version with respect to the meridian plane across the optical axis and the off-axis point, which leads to reflection symmetric PSFs, as shown in Fig. 1(b).

Note that the local reflection symmetry, which states that the local PSF at location $\mathbf{x}$ is reflection symmetric with respect to the line connecting the principle point and $\mathbf{x}$, has already been utilized in Schuler *et al*. [13]'s algorithm. However, this constraint fits the off-axis PSFs very well, but does not apply to the near-axis PSFs. Therefore, in this paper, we propose a more general constraint addressing both cases. Specifically, in our radial split framework, the PSF of the center patch (a solid circle witgh no warping) is constrained to be central symmetric, while the reflection symmetry constraint is applied for the PSFs in the outer rings.

Next, we formulate these two symmetry constraints in a unified mathematical term. The basic idea is to divide the PSFs into sets according to the specific type of symmetry, and then minimize the summation of intra-set variances. Mathematically it is defined as:

$$\mathcal{C}^k_{sym}(\mathbf{K}) = \lambda_s \sum_j \sum_{i \in \mathbb{S}_j} (\mathbf{K}(i) - \frac{1}{|\mathbb{S}_j|} \sum_{m \in \mathbb{S}_j} \mathbf{K}(m))^2, \quad (1)$$

where $\mathbf{K}$ denotes the PSF, j indices the sets $\mathbb{S}_j$ whose size is $|\mathbb{S}_j|$, and i is the index of the elements in a set. The weight of symmetry constraint λ_s is set to be 20 in this paper.

For reflection symmetry, we force each entry of the PSF to be the same as its reflection counterpart:

$$\mathcal{C}^k_{sym}(\mathbf{K}) = \lambda_{rs} \sum_{x,y} (\mathbf{K}(x,y) - \frac{1}{2}(\mathbf{K}(x,y) + \mathbf{K}(-x,y)))^2, \quad (2)$$

where (x, y) is the 2D Cartesian coordinate of the PSF, and $(-x, y)$ is the corresponding reflection symmetric coordinate with respect to the y-axis.

For the central symmetric PSFs near the optical axis, the symmetry constraint becomes:

$$\mathcal{C}^k_{sym}(\mathbf{K}) = \lambda_{cs} \sum_{r,\theta} (\mathbf{K}(r,\theta) - \frac{1}{|\Theta|} \sum_{\theta} \mathbf{K}(r,\theta))^2, \quad (3)$$

where (r, θ) is the polar coordinate, and $|\Theta|$ is the number of quantization levels of angular coordinate θ. In this paper, we uniformly samples 16 angles from 0^o to 360^o.

3. Visual Priors

In this section, we investigate image priors in the aberration corrupted images. By collecting and examining a large number of images captured by multiple types of consumer-level devices, e.g. mobile phones, pocket cameras, and single lens reflex cameras, we found that almost all the lenses are designed to have good imaging quality in the center region of the image, and also in a certain color channel, which usually is the green channel. Besides, the aberration PSFs vary smoothly in the spatial domain. According to these facts, our approach uses the relationships among the image channels and adjacent PSFs to improve the overall aberration correction performance.

In this work, after radial splitting and warping, we use the Normalized Sparsity Measure (NSM) L_1/L_2 (see [8] for details) to measure the sharpness of each channel of the warped image patches. Intuitively, it is easier to restore a

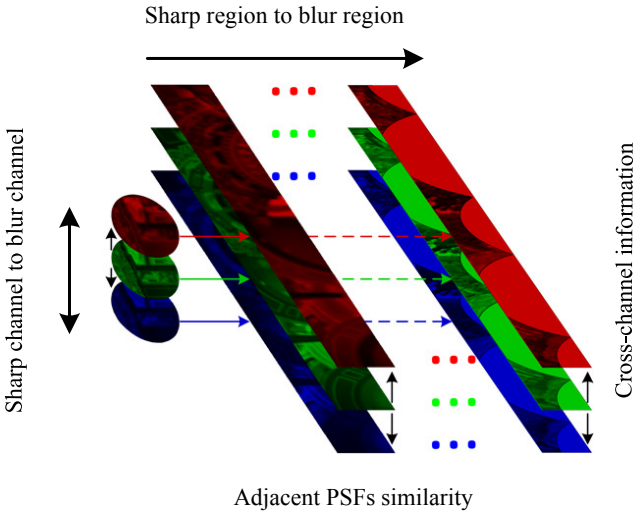

Figure 3. Diagram of the proposed sharp-to-blur strategy.

sharper image than a more blurry one by blind deconvolution, due to the smaller amount of lost frequencies and reduced illposedness. Therefore, we propose a sharp-to-blur strategy for lens aberration removal. As shown in Fig. 3, the sharp-to-blur strategy consists of two main information propagation directions: (1) from a sharp channel to more blurry channels for non-blind image deconvolution, and (2) from sharp regions to more blurry ones for PSF estimation. These two steps will be described in detail in the following.

Sharp-Channel Prior For images capturing nature scenes, discontinuities in different color channels (RGB or multispectrum) usually occur at the same positions, especially pixels on image edges. This property is extensively used as cross-channel constraint in various image reconstruction tasks, such as denoising [6] and non-blind aberration removal [3]. However, in these methods all the color channels are processed together, thus complex optimization algorithms (e.g. Iteratively Reweighted Least Squares (IRLS) and Optimal First-Order Primal-Dual (OFOPD)) are needed. Although these methods can achieve good results, the high computational cost hampers their applicability in blind deconvolution, where the non-blind deconvolution procedure needs to be repeatedly applied for kernel estimation.

In this paper, we propose to restore the sharpest channel first, and then use it as the reference channel to restore the other ones. Specifically, for an image region p to be restored, its sharpest channel sc is determined by selecting the one with the smallest NSM. For the sharpness channel $ch = sc$, we set $\mathcal{C}_{sc}(\mathbf{L}_{p,sc}) = \lambda_l||\nabla\mathbf{L}_{p,sc}||_1$ as the smoothness constraint in deconvolution ($\mathbf{L}_p$ denotes the latent sharp image patch p). For other channels (i.e. $ch \neq sc$), the result of the sharpest channel is used as a reference for restoration as:

$$\mathcal{C}_{ch}(\mathbf{L}_{p,ch}) = \lambda_l||\nabla\mathbf{L}_{p,ch}||_1 + \lambda_{ch}||\nabla\mathbf{L}_{p,ch} - \nabla\mathbf{L}_{p,ref}||, \tag{4}$$

where $\nabla\mathbf{L}_{p,ref}$ is the scaled gradient map of the sharpest channel defined as:

$$\nabla\mathbf{L}_{p,ref} = sign(\nabla\mathbf{B}_{p,ch}\nabla\mathbf{B}_{p,sc})\frac{|\nabla\mathbf{B}_{p,ch}|\nabla\mathbf{L}_{p,sc}}{|\nabla\mathbf{B}_{p,sc}| + \epsilon}. \tag{5}$$

where $\nabla\mathbf{B}_{p,ch}$ and $\nabla\mathbf{L}_{p,ch}$ are the gradients of observed and restored single channel image patch p, ϵ is a small constant to prevent the denominator to be zeros and is set to be 0.01 in our system.

Spatially-constrained Kernel Estimation Schuler *et al.* [13] assume that PSFs vary smoothly and their size is scaled linearly with the distance to the image center. However the linear scale assumption fails for the combined aberrations. In this work we relax this assumption by only assuming high similarity between the PSF of a patch and that of its neighboring patch under a simple transform. Based on this assumption while adopting the sharp-to-blur strategy, we propose to use the transformed version of the PSF computed from the previous sharper patch as the reference for the current patch, which leads to the following energy term:

$$C^k_{adj}(\mathbf{K}) = \sum_p \lambda^{k_p}_{adj}||\mathbf{K}_p - \mathcal{T}_{p-1\to p}\cdot\mathbf{K}_{p-1}||^2, \tag{6}$$

where $\mathcal{T}_{p-1\to p}$ is the transformation between adjacent PSFs defined as:

$$\mathcal{T}_{p-1\to p} = \mathcal{W}_{r_p}\cdot\mathcal{W}^{-1}_{r_{p-1}}, \tag{7}$$

where $\mathcal{W}_{r_p}$ is the warping of the p-th concentric radial region from the origional image space to the rectangle subimage, and $\mathcal{W}^{-1}_{r_{p-1}}$ is the inverse warping of the $(p-1)$-th subimage from the rectangle subimage space to the origional image space. Practically, we put the kernel of the $(p-1)$-th subimage at $(r_{p-1}, -90^o)$, warp it back to the original image, move it to $(r_p, -90^o)$, and then warp the kernel to the p-th subimage.

4. Optimization

Incorporating both the geometric and visual priors, our final objective function for aberration removal is:

$$E = \sum_p \{\ ||\mathbf{L}_p * \mathbf{K}_p - \mathbf{B}_p||^2 + \mathcal{C}^l_{ch}(\mathbf{L}_p) + \mathcal{C}^k_{sym}(\mathbf{K}_p) + \mathcal{C}^{k_p}_{adj}(\mathbf{K}_p, \mathbf{K}_{p-1})\ \}, \tag{8}$$

where $\mathbf{B}_p$ and $\mathbf{L}_p$ are the observed and restored image patch p. We now describe how to optimize this objective function.

4.1. Kernel Estimation

In the kernel estimation step, we follow the sharp-to-blur strategy to estimate the kernels from subimages sequentially. For a specific region p, $\mathcal{C}_{adj}^{k_p}(\mathbf{K}_p, \mathbf{K}_{p-1})$ is quadratic, and thus can be computed by pixelwise division in Fourier domain, together with the data term. To apply the symmetry constraint $\mathcal{C}_{sym}^{k}(\mathbf{K}_p)$, an auxiliary variable $\mathbf{Q}$ is introduced, and the energy function becomes:

$$\begin{aligned} E(\mathbf{K}_p) = &||\mathbf{L}_p * \mathbf{K}_p - \mathbf{B}_p||^2 + \mathcal{C}_{adj}^{k_p}(\mathbf{K}_p, \mathbf{K}_{p-1}) \\ &+ \beta||\mathbf{K}_p - \mathbf{Q}||^2 + \mathcal{C}_{sym}^{k}(\mathbf{Q}), \end{aligned} \tag{9}$$

where β is a weighting factor increasing with iteration. In our implementation, β is initialized as 20, and doubles in each iteration. Specifically, Eq. 9 can be minimized by iteratively solving two subproblems,

$$\begin{aligned} a) \quad \mathbf{K}_p^{t+1} = &\arg\min_{\mathbf{K}_p} ||\mathbf{L}_p * \mathbf{K}_p - \mathbf{B}_p||^2 + \beta||\mathbf{K}_p - \mathbf{Q}^t||_2^2 \\ &+\lambda_{adj}^{k_p}||\mathbf{K}_p - \mathbf{K}_{ref}||_2^2, \\ b) \quad \mathbf{Q}^{t+1} = &\arg\min_{\mathbf{Q}} \mathcal{C}_{sym}^{k}(\mathbf{Q}) + \beta||\mathbf{K}_p^{t+1} - \mathbf{Q}||_2^2, \end{aligned} \tag{10}$$

until the algorithm converges when the quadratic sum of update errors is smaller than 1e-6. Here, $\mathbf{K}_{ref} = \mathcal{T}_{p-1\to p} \cdot \mathbf{K}_{p-1}$. Empirically, the algorithm usually converges in less than 10 iterations. The first sub-problem can be solved in Fourier domain as:

$$\mathbf{K}_p^{t+1} = \mathcal{F}^{-1}\left(\frac{\mathcal{F}(\mathbf{L}_p)^*\mathcal{F}(\mathbf{B}_p) + \beta\mathcal{F}(\mathbf{Q}^t) + \lambda_{adj}^{k_p}\mathcal{F}(\mathbf{K}_{ref})}{\mathcal{F}(\mathbf{L}_p)^*\mathcal{F}(\mathbf{L}_p) + \beta + \lambda_{adj}^{k_p}}\right) \tag{11}$$

where $\mathcal{F}(\cdot)$ is the Fourier transform, and * is the complex conjugate operation. The second sub-problem only refers to the symmetry constraint, and there exists a closed-form solution in the case of either reflection or central symmetry.

As for reflection symmetry, Eq. $10-b$) can be divided into a series of two-tuples and each tuple contains only a pair of points that have reflection symmetry. The solution of sub-problem b) can be achieved by optimizing all the two-tuples individually. For a single two-tuple, the optimization objective is:

$$\begin{aligned} \arg\min_{Q_{ij}, Q_{i'j'}} E(Q_{ij}, Q_{i'j'}) = &\lambda_{rs}(Q_{ij} - Q_{i'j'})^2 \\ &+ \frac{1}{4}\beta(Q_{ij} - K_{ij})^2 + \frac{1}{4}\beta(Q_{i'j'} - K_{i'j'})^2 \end{aligned} \tag{12}$$

where Q_{ij}, $Q_{i'j'}$, K_{ij} and $K_{i'j'}$ are the abbreviations for $\mathbf{Q}(i,j)$, $\mathbf{Q}(i',j')$, $\mathbf{K}(i,j)$ and $\mathbf{K}(i',j')$ respectively. To optimize Eq. 12, we set its partial derivative to be zero:

$$\begin{aligned} \frac{\partial E}{\partial Q_{ij}} &= 2\lambda_{rs}(Q_{ij} - Q_{i'j'}) + \frac{1}{2}\beta(Q_{ij} - K_{ij}) = 0 \\ \frac{\partial E}{\partial Q_{i'j'}} &= -2\lambda_{rs}(Q_{ij} - Q_{i'j'}) + \frac{1}{2}\beta(Q_{i'j'} - K_{i'j'}) = 0 \end{aligned} \tag{13}$$

and derive the closed form solution as:

$$\begin{aligned} Q_{ij} &= \frac{(\beta/4\lambda_{rs} + 1)K_{ij} + K_{i'j'}}{2 + \beta/4\lambda_{rs}} \\ Q_{i'j'} &= \frac{(\beta/4\lambda_{rs} + 1)K_{i'j'} + K_{ij}}{2 + \beta/4\lambda_{rs}}, \end{aligned} \tag{14}$$

which can be calculated efficiently.

In the case of central symmetry, to solve subproblem b), we also divide Eq. $10-b$) into a series of tuples with the elements coupled together fall in the same tuple. The single tuple objective function is:

$$\arg\min_{Q_{r\theta}|_{\theta\in\Theta}} E(Q_r) = \lambda_{rs}\sum_{\theta\in\Theta}(Q_{r\theta} - \overline{Q_r})^2 + \beta(Q_{r\theta} - K_{r\theta})^2, \tag{15}$$

where $\overline{Q_r}$ denotes the average with respect to θ. By setting its partial derivative $\frac{\partial E(Q_{r\theta})}{\partial Q_{r\theta}}|_{\theta\in\Theta}$ to be zero, Eq. 16 can be optimized by solving a linear equation system,

$$\begin{bmatrix} \frac{(|\Theta|-1)^2}{|\Theta|} + \frac{\beta}{\lambda_{cs}} & \frac{(1-|\Theta|)}{|\Theta|} & \cdots \\ \frac{(1-|\Theta|)}{|\Theta|} & \frac{(|\Theta|-1)^2}{|\Theta|} + \frac{\beta}{\lambda_{cs}} & \cdots \\ \vdots & \vdots & \ddots \end{bmatrix} = \frac{\beta}{\lambda_{cs}} \begin{bmatrix} K_{r\theta_1} \\ K_{r\theta_2} \\ \vdots \end{bmatrix}. \tag{16}$$

In our implementation we set $|\Theta| = 16$.

4.2. Non-blind Deconvolution

In the final non-blind deconvolution step, we compute the latent image sequentially on color channels according to the sharp-to-blur strategy. For a single image patch, the objective function is:

$$E(\mathbf{L}_p) = ||\mathbf{L}_p * \mathbf{K}_p - \mathbf{B}_p||^2 + \mathcal{C}_{ch}^{l}(\mathbf{L}_p). \tag{17}$$

where $\mathbf{B}_{p,ch}$ and $\mathbf{L}_{p,ch}$ are the observed and restored single channel image patch p. The fast iterative shrinkage/thresholding algorithm (FISTA) [7, 19] is applied to solve the sharpest channel of $\mathbf{L}_p$. For other channels, the reference part $\nabla\mathbf{L}_{p,ref} = sign(\nabla\mathbf{B}_p^{ch} \cdot \nabla\mathbf{B}_p^{sc})\frac{|\nabla\mathbf{B}_p^{ch}|\nabla\mathbf{L}_p^{sc}}{|\nabla\mathbf{B}_p^{sc}|+\epsilon}$ in Eq. 4 is constant after solving the sharp channel. By extending Krishnan and Fergus [7]'s algorithm, we split

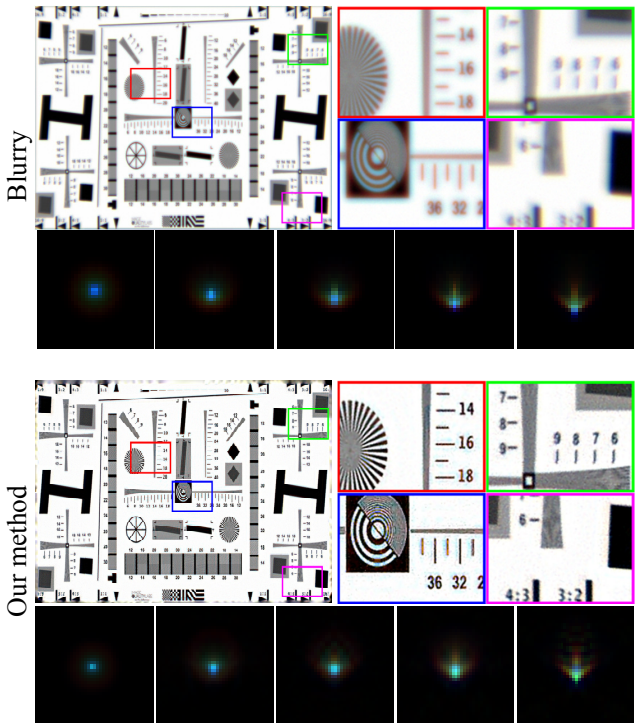

Figure 4. Top: a synthetic image generated by simulating the light transport of a single biconvex lens, with ground-truth blur kernels in high-lighted regions. Bottom: recovered latent image and PSFs by our algorithm.

Eq. 17 into two sub-problems:

$$
\begin{aligned}
a) \quad \mathbf{L}_{p,ch}^{t+1} &= \arg\min_{\mathbf{L}_{p,ch}} ||\mathbf{L}_{p,ch} * \mathbf{K}_{p,ch} - \mathbf{B}_{p,ch}||^2 \\
&\quad + \beta||\nabla\mathbf{L}_{p,ch} - \mathbf{Z}_{p,ch}^t||_2^2 \\
b) \quad \mathbf{Z}_{p,ch}^{t+1} &= \arg\min_{\mathbf{Z}_{p,ch}} \lambda_{ch}||\mathbf{Z}_{p,ch}^t - \nabla\mathbf{L}_{p,ref}||_1 \\
&\quad + \lambda_l||\mathbf{Z}_{p,ch}^t||_1 + \beta||\nabla\mathbf{L}_{p,ch}^{t+1} - \mathbf{Z}_{p,ch}^t||_2^2.
\end{aligned} \tag{18}
$$

where $\mathbf{Z}_{p,ch}$ is the auxiliary variable (another version of $\nabla\mathbf{L}_{p,ch}$), $\nabla\mathbf{L}_{p,ref}$ is the scaled gradient of deconvolved sharpest channel defined in Eq. 5.

The sub-problem a) of Eq. 18 can be computed by the pixelwise division in Fourier domain. To solve sub-problem b), we form a 2-D lookup table by recording the minimum $\mathbf{Z}_{p,ch}$ with given $\nabla\mathbf{L}_{p,ch}$ and $\nabla\mathbf{L}_{p,ref}$. In practice, both $\nabla\mathbf{L}_{p,ch}$ and $\nabla\mathbf{L}_{p,ref}$ are uniformly sampled from -1 to 1 with 100 samples, and the minimum solution of Eq. 18 b) with each combination of $\nabla\mathbf{L}_{p,ch}$ and $\nabla\mathbf{L}_{p,ref}$ are computed numerically, i.e., a 2-D lookup table with 100×100 entries are formed. The minimization of Eq. $18-b$) can be achieved efficiently by searching the lookup table. Note that the weights λ_l and λ_{ch} are constant, but β increases with iteration, so for each β we need to build a separate 2-D lookup table. Fortunately, β needs to be updated only several times during the whole algorithm, so a few Mega-bytes memory block is sufficient for storing all the tables.

Figure 5. Comparison on the image captured by Sony Cyber-shot DSC-P93A 8mm f/5.6 lens.

5. Experiment Results

We verify our algorithm on a variety of images, including both synthetic and real-world data, and compare the results with state-of-the-art algorithms.

A synthetic example. We test the proposed algorithm on a synthetic image generated by tracing the light rays across a biconvex lens camera, as shown in Fig. 4(top), which is severely degraded by various aberrations such as spherical aberration, coma aberration and chromatic aberration. The recovered latent image as well as PSFs of our algorithm are shown in Fig. 4(bottom). The result shows that the proposed algorithm achieves high quality result in all image areas and can correct all types of aforementioned aberrations.

In terms of computational efficiency, the proposed algorithm processes each of the images in Fig. 4 (1024*768 pixels) within around 1.5 minutes, using our Matlab implementation on a PC with Intel Core i5 CPU at 3.2GHz and 8G RAM.

Comparisons on real data. We apply the proposed method on real captured images as shown in Fig. 5, 6, 7 and 8. Comparisons with various state-of-the-art algorithms

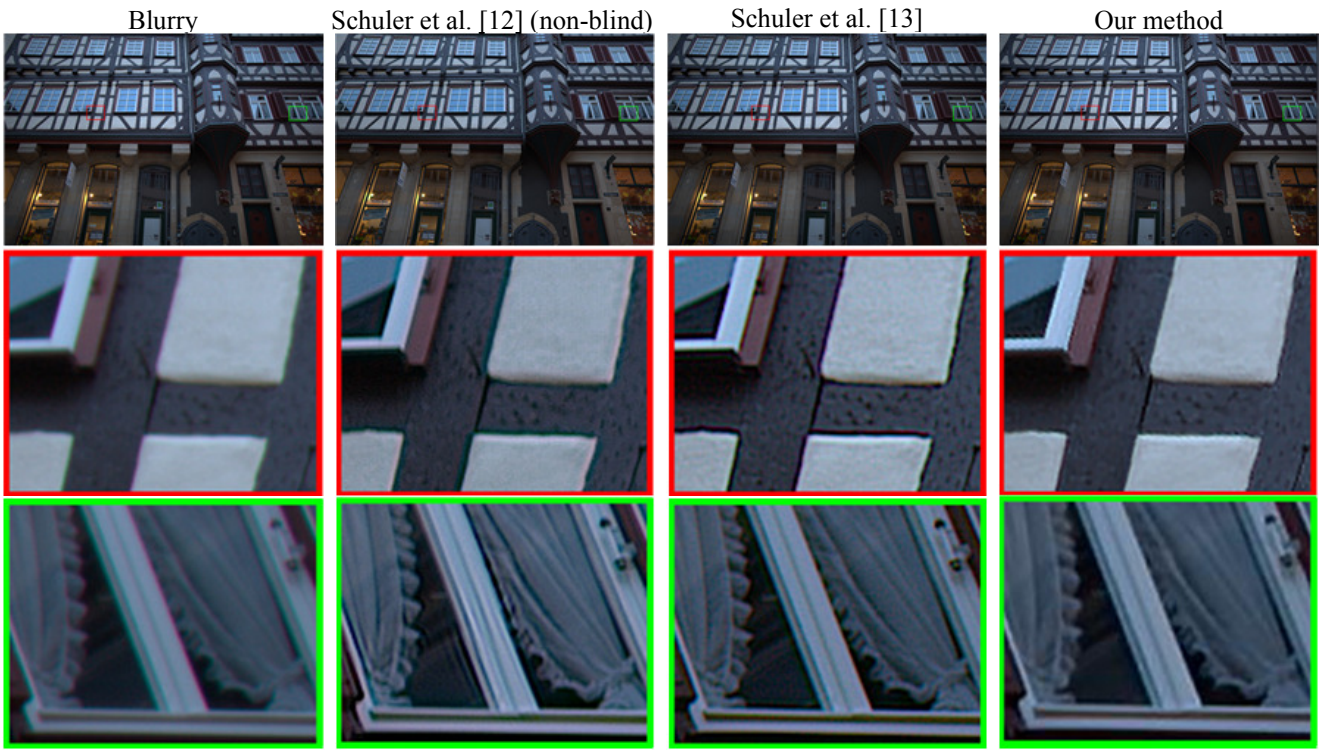

Figure 6. Comparison on an image captured by a Canon 24mm f1/4 lens (provide by Schuler *et al*. [12]).

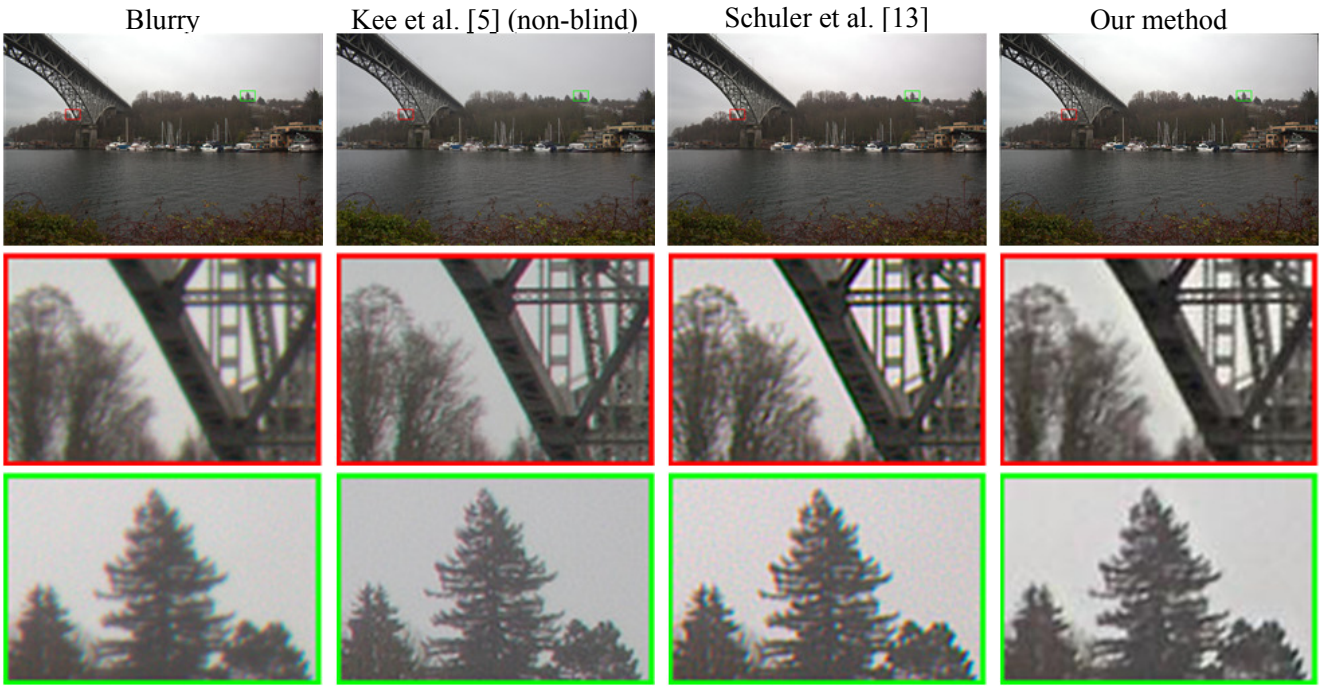

Figure 7. Comparison on an image captured by a Canon Rebel T2i at 18mm f/3.5 (provide by Kee *et al*. [5]).

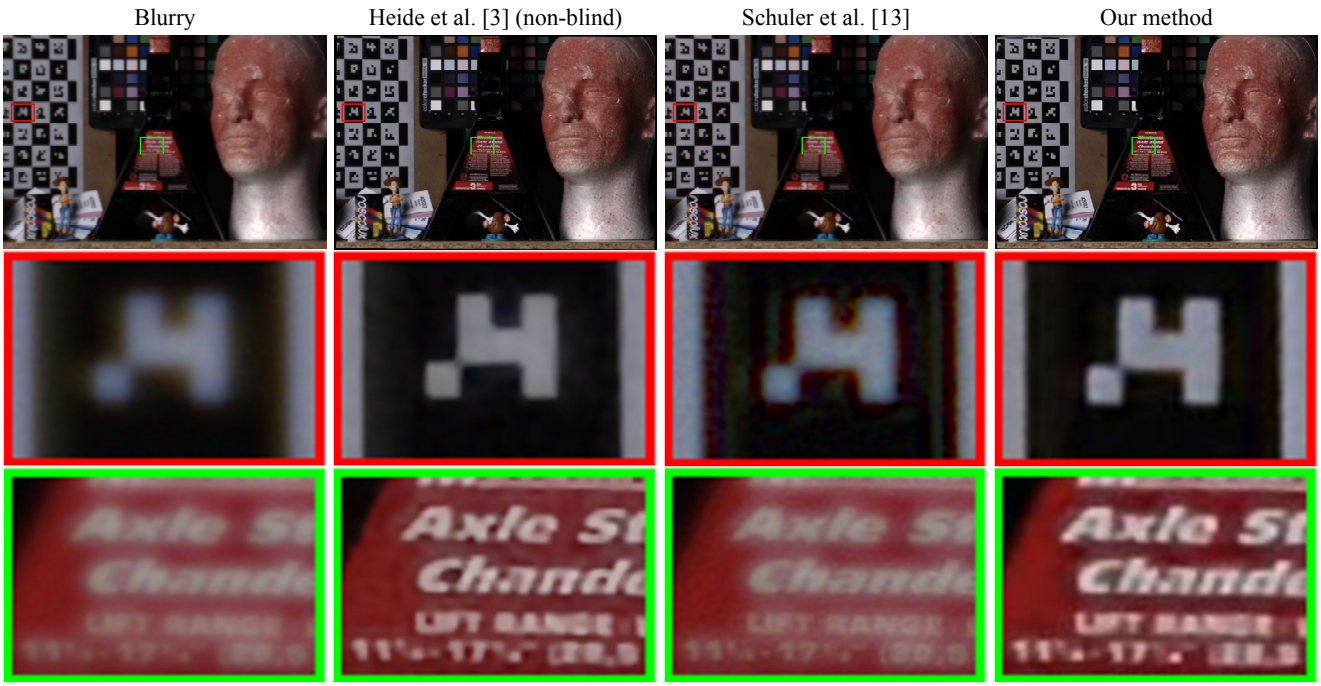

Figure 8. Comparison on an image captured by a simple lens camera (provide by Heide *et al*. [3]).

are provided in these figures.

The input image in Fig. 5 is captured by a consumer pocket camera (Sony Cyber-shot DSC-P93A 8mm f/5.6 lens), and the chromatic aberration is the main source of deterioration of this image. The result of Schuler *et al*. [13] and ours are shown in the middle and bottom row, respectively. We see that the proposed approach achieves a little sharper result at the image center, while removes the chromatic aberration much better at the bottom-right corner of the image.

In both Fig. 6 and Fig. 7, the input images are captured by Single-lens reflex (SLR) cameras. We see that our algorithm produces higher quality results than the state-of-the-art methods, even the non-blind ones (Schuler *et al*.'s [12] and Kee *et al*.'s [5]). Benefiting from the proposed sharp-to-blur strategy, our method generates significantly higher quality results especially in regions with large chromatic aberrations, because the sharpest channel can offer more additional information for the deconvolution of the rest channels in these case.

Fig. 8 shows comparisons on an aberrated image provided by Heide *et al*. [3]. It is a challenging example for its extremely large blur. We see that our result is only slightly worse than that of the non-blind algorithm [3], but is much better than that of Schuler *et al*. [13]. The inferior recovery by [13] is due to the fact that their assumption on PSFs does not hold in this case with spherical aberration, meanwhile, our algoirthm can handle the near-axis PSFs very well by utilizing the central symmetry constraint. Besides, the proposed algorithm makes full use of the cross-channel information and the smoothly-varying kernel constraint to derive the promising result in the off-axis regions.

6. Conclusion and Discussions

In this paper, we propose a new blind deconvolution approach that utilizes and incorporates various geometric and visual priors for optical aberration removal from a single image. Our method includes a novel radial splitting and warping framework to convert the non-uniform blur problem into multiple uniform ones, and a sharp-to-blur strategy for improved performance and robustness. Comparisons with the state-of-the-art algorithms verify the effectiveness of the proposed algorithm.

The proposed algorithm is robust against small noise due to the L_1 sparse prior and cross-channel constraint. For the same reason, the approach is also robust to minor compression artifacts. However, severe nonlinear camera response may cause the algorithm to fail, since the image formation model is essentially linear.

As future work, we plan to explore how to jointly correct optical aberrations from multiple images captured by the same camera.

Acknowledgements

This work was supported by the Project of NSFC (No. 61327902, 61120106003, 61371166, 61422107 and 61171119).

References

[1] P. Bedggood, R. Ashman, G. Smith, and A. Metha. Multi-conjugate adaptive optics applied to an anatomically accurate human eye model. *Opt. Express*, 14(18):8019–8030, 2006.

[2] S. Cho and S. Lee. Fast motion deblurring. *ACM Trans. Graph.*, 28(5):1, Dec. 2009.

[3] F. Heide, M. Rouf, M. B. Hullin, B. Labitzke, W. Heidrich, and A. Kolb. High-quality computational imaging through simple lenses. *ACM Trans. Graph.*, 32(5):149:1–149:14, Oct. 2013.

[4] N. Joshi, R. Szeliski, and D. Kriegman. PSF estimation using sharp edge prediction. In *CVPR*, June 2008.

[5] E. Kee, S. Paris, S. Chen, and J. Wang. Modeling and removing spatially-varying optical blur. In *ICCP*, April 2011.

[6] D. Krishnan and R. Fergus. Dark flash photography. *ACM Transactions on Graphics, SIGGRAPH 2009 Conference Proceedings*, page To appear, 2009.

[7] D. Krishnan and R. Fergus. Fast Image Deconvolution using Hyper-Laplacian Priors. In *NIPS*, 2009.

[8] D. Krishnan, T. Tay, and R. Fergus. Blind deconvolution using a normalized sparsity measure. In *CVPR*, pages 233–240, June 2011.

[9] E. Logean, E. Dalimier, and C. Dainty. Measured double-pass intensity point-spread function after adaptive optics correction of ocular aberrations. *Opt. Express*, 16(22):17348–17357, 2008.

[10] L. Mugnier, J.-F. Sauvage, T. Fusco, A. Cornia, and S. Dandy. On-line long-exposure phase diversity: a powerful tool for sensing quasi-static aberrations of extreme adaptive optics imaging systems. *Opt. Express*, 16(22):18406–18416, 2008.

[11] K. Rahbar and K. Faez. Blind correction of lens aberration using zernike moments. In *ICIP*, pages 861–864, 2011.

[12] C. Schuler, M. Hirsch, S. Harmeling, and B. Scholkopf. Non-stationary correction of optical aberrations. In *ICCV*, pages 659–666, Nov 2011.

[13] C. Schuler, M. Hirsch, S. Harmeling, and B. Schölkopf. Blind correction of optical aberrations. In *ECCV*, pages 187–200. 2012.

[14] Y. Shih, B. Guenter, and N. Joshi. Image enhancement using calibrated lens simulations. In *ECCV*, volume 7575, pages 42–56. 2012.

[15] H. Song, R. Fraanje, G. Schitter, H. Kroese, G. Vdovin, and M. Verhaegen. Model-based aberration correction in a closed-loop wavefront-sensor-less adaptive optics system. *Opt. Express*, 18(23):24070–24084, 2010.

[16] H. Tang and K. N. Kutulakos. What does an aberrated photo tell us about the lens and the scene? In *ICCP*, pages 1–10. IEEE, 2013.

[17] T. Vettenburg and A. R. Harvey. Holistic optical-digital hybrid-imaging design:wide-field reflective imaging. *Appl. Opt.*, 52(17):3931–3936, Jun 2013.

[18] K. Wang, D. E. Milkie, A. Saxena, P. Engerer, T. Misgeld, M. E. Bronner, J. Mumm, and E. Betzig. Rapid adaptive optical recovery of optimal resolution over large volumes. *Nature Methods*, 11:625–628, Apr. 2014.

[19] Y. Wang, J. Yang, W. Yin, and Y. Zhang. A new alternating minimization algorithm for total variation image reconstruction. *SIAM J. Imaging Sci.*, pages 248–272, 2008.

[20] T. Yue, J. Suo, Y. Xiao, L. Zhang, and Q. Dai. Image quality enhancement using original lens via optical computing. *Opt. Express*, 22(24):29515–29530, Dec 2014.